Perturbative transport studies in the reversed-field pinch

2005 Nucl. Fusion 45 1342

(http://iopscience.iop.org/0029-5515/45/11/015)

INSTITUTE OF PHYSICS PUBLISHING and INTERNATIONAL ATOMIC ENERGY AGENCY NUCLEAR FUSION

Nucl. Fusion **45** (2005) 1342–1349 doi:10.1088/0029-5515/45/11/015

Perturbative transport studies in the reversed-field pinch

L. Frassinetti[1], M. Gobbin[1,2], L. Marrelli[1], P. Piovesan[1], P. Franz[1], P. Martin[1,2] and B.E. Chapman[3]

[1] Consorzio RFX, Associazione EURATOM-ENEA sulla Fusione, Corso Stati Uniti, 4 35127 Padova, Italy
[2] Department of Physics, University of Padova, Padova, Italy
[3] Department of Physics, University of Wisconsin, 1150 University Avenue, Madison, Wisconsin 53706, USA

Received 24 February 2005, accepted for publication 18 August 2005
Published 24 October 2005
Online at stacks.iop.org/NF/45/1342

Abstract
In this paper we present the results of transient transport experiments in a reversed-field pinch device. Measurements have been made in the Madison Symmetric Torus experiment using a novel soft x-ray diagnostic. Spontaneous transient transport events are observed in enhanced confinement shots obtained using the pulsed parallel current drive technique, as a consequence of bursts of magnetic fluctuations triggered by an edge resonant $m = 0$ instability. The perturbed electron heat diffusivity, χ_e, is estimated through a numerical transient heat transport model, and the values thus obtained are compared with those measured in similar unperturbed enhanced confinement and standard plasmas using the power balance technique.

PACS numbers: 52.25.Fi, 52.55.Hc

(Some figures in this article are in colour only in the electronic version)

1. Introduction

The perturbation of an equilibrium state is a powerful technique complementary to power balance for the study of heat and particle transport in magnetized fusion devices [1, 2]. Perturbative experiments and their theoretical modelling have allowed in recent years the comprehension of many aspects of anomalous transport in thermonuclear plasmas, mainly in tokamaks and stellarators. Spontaneous transient transport phenomena are observed as a consequence of sawtooth crashes, edge-localized modes, or other magnetohydrodynamic (MHD) events [3–5]. Methods for the active induction of heat and cold pulses have also been developed, which permit one to probe the plasma in a more controlled and less perturbative way. These make use, for example, of localized radio frequency heating, laser blow-off of impurities, or shallow injection of pellets [6–8]. Complex transport phenomena like non-local or ballistic heat and cold pulse propagation have been observed in these experiments [9, 10]. An explanation in terms of critical gradient theories of plasma turbulence has been proposed, and a number of aspects can be interpreted in this framework [11, 12]. Nevertheless, the understanding of transport phenomena in plasmas is incomplete and awaits improvements in diagnostic and theory, as well as an enlargement of the experimental database.

In this paper we report a study of transient transport phenomena in the Madison Symmetric Torus (MST) [13] reversed-field pinch (RFP) experiment [14], with some previous observations having been reported in MST [15] and ZT-40 [16, 17]. Spontaneous transient transport events have been observed in MST during enhanced confinement regimes achieved through the so-called pulsed parallel current drive (PPCD) technique [18, 19]. Measurements have been made using a novel soft x-ray (SXR) diagnostic [20]. We show in this paper that, as done before in tokamaks and stellarators [1, 2], perturbative techniques provide a tool for studying heat transport in the RFP. In addition, the evidence that this tool can be applied to the RFP opens the possibility of a detailed comparison of the physics of heat conduction in the main configurations for the confinement of magnetized plasmas. It is also important to stress that, by applying this method in MST, an estimate of χ_e in perturbed PPCD plasmas has been obtained, which reinforces the confidence in the relevance of the PPCD scenario for obtaining improved confinement regimes.

Heat and particle transport in the standard RFP is dominated by magnetic fluctuations [21]. Recently, transient inductive modification of the current density profile through the PPCD technique has allowed a strong reduction of magnetic turbulence and, as a result, a record improvement of

energy confinement up to levels comparable with similar size tokamaks [22]. Clear experimental evidence of a significant magnetic chaos reduction in the RFP has been reported [23,24], and power balance estimates of the electron heat diffusivity, χ_e, indicate values as low as 5–10 $m^2\ s^{-1}$ during unperturbed PPCD shots.

Confinement in these plasmas is occasionally degraded by bursts of broadband magnetic fluctuations, which are triggered by edge resonant $m = 0$ modes [19]. These events are distinct from normal sawtooth crashes observed in standard plasmas, where $m = 1$ modes grow at first and $m = 0$ modes follow [25]. MHD bursts in enhanced confinement plasmas are associated with fast relaxation of the SXR radial profile and expulsion of thermal energy towards the plasma edge. Heat transport in this situation has been modelled with a diffusive heat transport model, which includes features specific to the RFP configuration. Using this model, we estimate the perturbed electron heat diffusivity, χ_e, during these events. The χ_e values thus obtained are about ten times higher than those estimated using the power balance method in unperturbed plasmas. Such a discrepancy was also observed in perturbative experiments performed in tokamaks [1,2] and will be discussed more deeply in the following.

2. Experimental evidence of transient transport events in MST

MST is a RFP experiment with major radius $R_0 = 1.5$ m and minor radius $a = 0.52$ m [13]. Two examples of MST shots representative of those analysed in this work are reported in figure 1: figures 1(*a*)–(*d*) and figures 1(*e*)–(*h*) represent, PPCD shots without and with MHD bursts, respectively. All the shots considered in the present work are characterized by a maximum plasma current $I_p \simeq 400$ kA and electron density $n_e \simeq 1 \times 10^{19}\ m^{-3}$. PPCD is applied at $t = 10$ ms and lasts for about 10 ms. This is visible from figures 1(*a*) and (*e*), where we report the surface electric field parallel to the equilibrium magnetic field $E_\parallel(a) = \boldsymbol{E} \cdot \boldsymbol{B}/B$. Note in particular the five $E_\parallel$ pulses associated with PPCD.

The application of PPCD is responsible for a strong reduction in the magnetic fluctuation amplitude, as is evident from figure 1(*b*) for a shot without MHD bursts: the wavelet spectrum of the dB/dt signal from a fast magnetic pick-up probe (frequency resolution up to 1500 kHz) shows that magnetic fluctuations are strongly reduced during PPCD over a broad frequency range. Shots with MHD bursts show instead that the magnetic fluctuation amplitude sharply increases during these events at many different frequencies (figure 1(*f*)). Nevertheless, during periods far from MHD bursts we observe that the magnetic activity is similar to that in shots without bursts. In both cases, a coherent frequency appears in the spectrum at about 20 kHz, which is produced by the rotation of an ($m = 1, n = 6$) dominant tearing mode. No evidence has been found of a correlation between the dynamics of this mode and the events studied in this paper. As shown in previous work [19], these events are strongly correlated with ($m = 0, n \geqslant 1$) modes, which are resonant at the reversal radius, r_{rev}, the radial position where the safety factor profile reverses its sign. This is located in the edge region at approximately $r_{rev} \simeq 0.38$ m. We observe in figure 1(*g*) that the average $m = 0$ mode

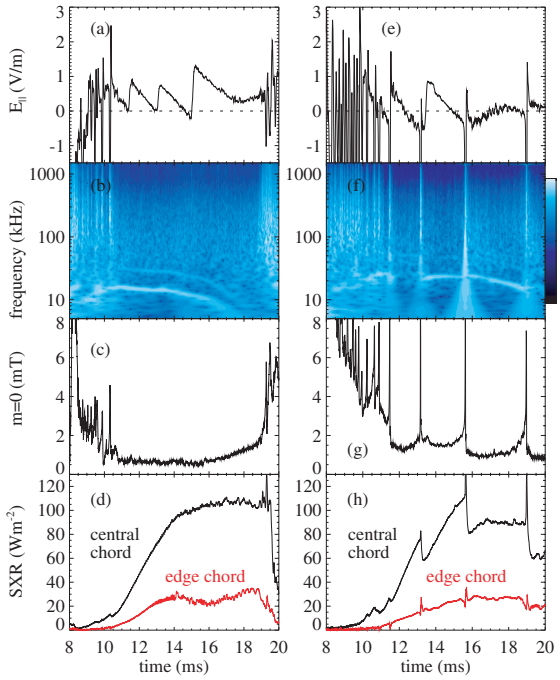

Figure 1. Examples of PPCD shots without (left column) and with (right column) MHD bursts. (*a*) and (*e*), surface parallel electric field; (*b*) and (*f*), wavelet spectrum of the dB/dt signal from a fast pick-up probe; (*c*) and (*g*), average amplitude of ($m = 0, n = 1$–4) modes; (*d*) and (*h*), SXR brightness from a central chord (black line) and an edge (red line) chord.

amplitude (toroidal component) transiently increases during MHD bursts, while it usually has a very low value, $\lesssim 1$ mT, in unperturbed PPCD shots (figure 1(*c*)). The SXR brightness measured by central chords is observed to increase soon after the application of PPCD at $t = 10$ ms (figures 1(*d*) and (*h*)). The growth of SXR emissivity mainly reflects an increase in electron temperature, which occurs despite a ∼50% drop in ohmic heating power [19]. MHD bursts are correlated with a sudden and transient loss of confinement, which is recorded as a fast drop in the SXR signal from the central chords. Just after the decrease in the SXR signal in the core, we observe an increase in the edge SXR chords (red line in figure 1(*h*)), which implies that an SXR pulse propagates outwards. After the magnetic event, the SXR brightness often recovers, as can be observed in figure 1(*h*).

The SXR diagnostic [20] used in the present work is composed of a pinhole photocamera with 12 chords. The radiation reaches an array of 12 photodiode detectors through a single pinhole and is filtered by a curved Be foil, which has a cut-off energy $E_c = 1200$ eV. The fan of chords is located at poloidal angle $\theta = 75^\circ$ (figure 2(*a*)). This diagnostic has a rather high bandwidth, $f \lesssim 100$ kHz, which makes it suitable for the study of fast events like those investigated in this paper. Figure 2(*b*) shows two SXR brightness radial profiles measured before (black symbols) and during (red symbols) a transient transport event. We can observe both the decrease in the SXR signal in the central chords and the increase in the four edge chords marked by vertical dotted lines, which will be used henceforth to study SXR pulse propagation. Note that the chord impact parameter, p, is computed with respect to the magnetic axis, which has a Shafranov shift $\Delta r \simeq 5$ cm.

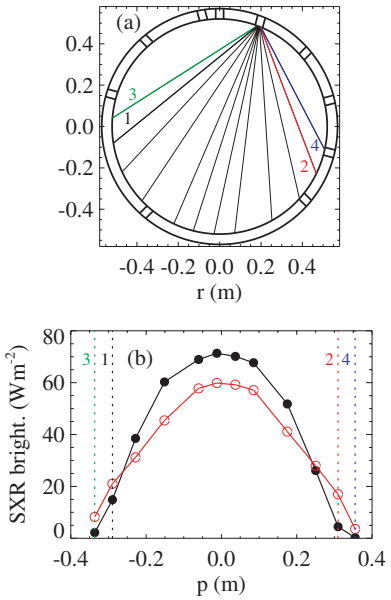

Figure 2. (*a*) Geometry of the SXR lines of sight in MST showing the fan at poloidal angle $\theta = 75^{\circ}$. (*b*) SXR brightness profiles corresponding to times before (black full symbols) and during (red open symbols) a transient transport event. Numbers on vertical dotted lines refer to the same four lines of sight as in figure (3).

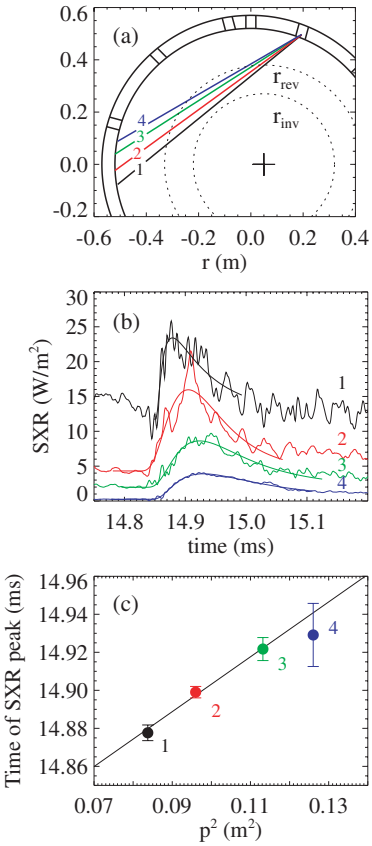

Figure 3. (*a*) Geometry of the four edge SXR chords. The outboard chords are mapped onto the inboard chord geometry. The reversal, $r_{\rm rev}$, and inversion, $r_{\rm inv}$, radii are indicated with dashed lines. (*b*) SXR brightness waveforms measured by the four edge SXR chords shown above during a transient transport event. The χ^2 fit made using the function defined in equation (1) is indicated with continuous smooth lines. (*c*) Time of SXR peaks corresponding to the SXR pulses shown in the above figure as a function of the impact parameter squared. The continuous line represents the linear fit. The same colour coding is used in all of the plots.

The edge chord geometry is shown in figure 3(*a*). The four edge chords are the same as those marked with vertical dotted lines in figure 2(*b*). Note that here we are plotting together two couples of chords with opposite impact parameter. In other words, we have mapped the outboard chords onto the inboard chords. The reversal radius $r_{\rm rev} \simeq 0.38\,$m and the inversion radius of the SXR radial profile $r_{\rm inv} \simeq 0.27\,$m are indicated in figure 3(*a*) with dotted lines. The inversion radius separates the core region, where the SXR profile decreases, from the edge region, where at the same time the profile increases. Figure 3(*b*) presents the waveforms of the SXR brightness measured by the four edge chords shown in figure 3(*a*). The time, $t_{\rm p}$, of SXR peaks measured by chords with increasing impact parameter confirms an outward propagation (the colour coding and the numbers are the same as those used in figure 3(*a*)).

Edge SXR signals have a relatively low amplitude and can be affected by a level of electromagnetic noise up to 20%. For this reason, in order to reduce the uncertainty in the determination of $t_{\rm p}$ from the SXR signals, we have used a Monte Carlo fitting method. We used the following pulse-shaped function to fit the signals:

$$f(t) = A \exp\left[-\frac{1}{2\gamma^2} \ln^2\left(\frac{t - t_0}{t_{\rm p}}\right)\right]. \qquad (1)$$

The results of the fit for the example in figure 3(*b*) are represented by continuous smooth lines. The fitting method we have adopted proceeds as follows. The initial time, t_0, at which the pulse starts is chosen, and then a code determines by χ^2 minimization the parameters $t_{\rm p}$, A and γ which best fit the SXR data. The error in these parameters is estimated by repeating many times the fit procedure on synthetic SXR signals obtained by adding to the experimental signal a different random noise with a relative amplitude of 20%. By this Monte Carlo procedure the sampling distribution of $t_{\rm p}$ is obtained: we find that this is Gaussian to a good approximation, and we use this information to obtain the best estimate of $t_{\rm p}$ together with its standard error, $\sigma_{t_{\rm p}}$.

In figure 3(*c*) we report the times of the SXR peaks, $t_{\rm p}$, determined using the above method as a function of the chord impact parameter squared, p^2. The result of a linear fit is also shown. The fit procedure takes into account the different $\sigma_{t_{\rm p}}$ standard errors for each point and computes the slope of the linear fit and its standard error. Note that we use here the impact parameter, p, of the SXR chords instead of the radial coordinate. This approximation is due to the line-integrated nature of the measurement and will be further investigated below. Due to the limited spatial resolution of the present measurements, other non-linear fits could also be compatible with the data. Thus, we cannot firmly comment at present on whether heat transport during these events is diffusive in nature.

In the next section we will develop a diffusive heat transport model, which will be used to interpret the approximately linear $t_{\rm p}$–p^2 relation. In this model the plasma is assumed to be in thermal equilibrium before a perturbation

is applied. The equilibrium will be chosen compatible with power balance measurements in MST PPCD plasmas. We will then make the basic assumption that χ_e is suddenly perturbed during transient transport events following an increased level of magnetic fluctuations, and the electron temperature profile is evolved accordingly. Since we lack at present a time resolved measurement of the electron temperature profile, the purpose of our model is not that of simulating single heat pulses with high resolution but rather to predict the general features of a large ensemble of similar events. For this reason, the model sensitivity to changes in the initial and boundary conditions will be tested, and an estimate of χ_e in perturbed PPCD plasmas will be thus obtained.

3. Numerical model of transient heat transport

3.1. Model thermal equilibrium

To interpret the transient transport events shown above, we have developed a diffusive model of transient heat transport. We have solved numerically the electron energy continuity equation in a cylinder with suitable initial and boundary conditions:

$$\frac{\partial}{\partial t}\left(\frac{3}{2}n_e T_e\right) = \frac{1}{r}\frac{\partial}{\partial r}\left(r n_e \chi_e \frac{\partial T_e}{\partial r}\right) + P_e. \qquad (2)$$

Here P_e represents the total electron power density, i.e. the sum of sources (ohmic deposition) and sinks (radiation) of power. Equation (2) has been numerically integrated using the method of lines [26]. We impose two boundary conditions to the electron temperature profile at each time instant: a null radial derivative, $\partial T_e/\partial r = 0$, at $r = 0$, and null electron temperature at the edge, $T_e(r = a) = 0$. The initial conditions to be specified are the radial profiles of the electron temperature, $T_{e0}(r)$, density $n_{e0}(r)$, total power density, $P_{e0}(r)$ and heat diffusivity, $\chi_{e0}(r)$, before the event.

The initial profiles have been chosen consistent with those measured in a series of 400 kA PPCD experiments similar to those analysed in the present work. In those experiments, in which a larger number of diagnostics were available, the T_e, n_e, P_e and χ_e profiles had been determined in unperturbed conditions through ensemble-averaging measurements taken in a series of many similar PPCD shots, and the power balance method was used to investigate the reduction in heat and particle transport due to PPCD (results are reported in [27]). The equilibrium profiles that have been used as initial conditions in the present model are shown in figure 4. Here we have chosen the electron temperature profile $T_{e0}(r) = T_0(1 - (r/a)^4)^3$ and the electron density profile $n_{e0}(r) = n_0(1-(r/a)^5)$. For simplicity we assume that the $\chi_{e0}(r)$ profile is constant throughout most of the plasma, with a sharp increase only at the very edge.

3.2. Basic model assumptions

In the present model we have assumed that the electron density, n_e, and the power density, P_e, profiles do not change in time during a transient transport event. The assumption on electron density is valid to a first approximation, since we have verified that the percentage perturbation in the core line-integrated

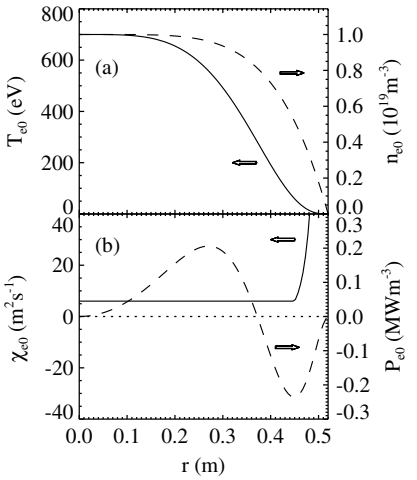

Figure 4. Equilibrium radial profiles used as initial conditions of the transient heat transport model. Radial profiles: (*a*) of the electron temperature, T_{e0}, and density, n_{e0}; (*b*) heat diffusivity, χ_{e0} and total power density, P_{e0}.

electron density during the events ($\Delta n_e \simeq$ 1–5%) is about ten times smaller than the corresponding perturbation in the core electron temperature ($\Delta T_e \simeq$ 10–30%), as measured using a double-filter technique similar to that described in [28].

Different contributions have to be considered for the P_e term. Resistive diffusion is expected to affect the current profile on a timescale much slower than that characteristic of transient transport events, given the relatively high electron temperature of PPCD plasmas. Its contribution to P_e should thus not vary much. Dynamo electric fields produced by coupled magnetic and flow velocity fluctuations [25] could affect the ohmic deposition profile during MHD bursts on fast timescales. A measurement of the dynamo electric field in high temperature PPCD plasmas is not yet available, and hence dynamo effects are not included consistently in the present model. The ohmic input power can vary on fast timescales during heat pulses due to the dependence of the resistivity on temperature. A sensitivity study of the model to variations in the ohmic input power with temperature will be presented in the following. This will show that the main model predictions are not significantly modified by such effects. Radiation losses do vary on a fast timescale, and their effect on the power balance is not negligible in PPCD plasmas, but we lack at present a complete characterization of the impurity content in these plasmas, and hence we have not included their variation in the time-dependent transport model.

3.3. Time evolution of thermal profiles

We evolve equation (2) by perturbing the χ_e profile with respect to the initial one. We make here the simplifying assumption that the χ_e profile during a transient transport event is suddenly increased by a single multiplicative factor throughout the plasma. More refined models, examining different χ_e radial profiles, will be the subject of future work. The model χ_e perturbation is shown in figure 5(*a*), where the black line represents the equilibrium $\chi_{e0}(r)$ profile, while the green line is the perturbed $\chi_e(r)$ profile during the burst. In figure 5(*d*)

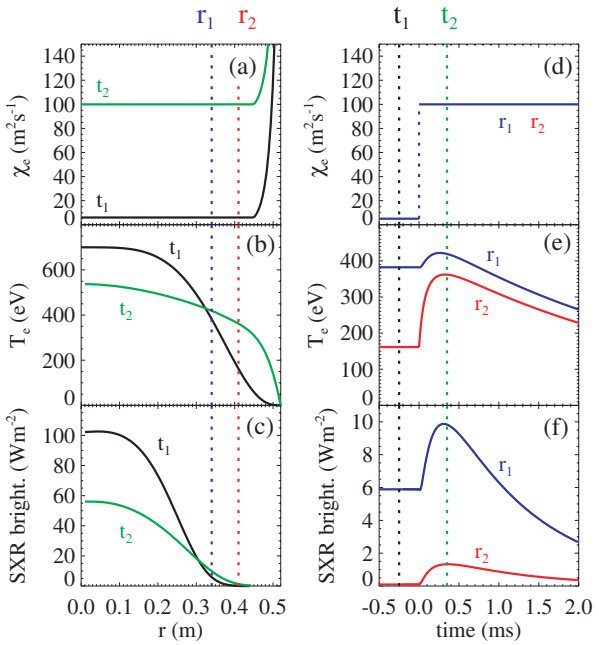

Figure 5. Results of the numerical transient heat transport model. (*a*) Equilibrium (black line) and perturbed (green line) χ_e radial profiles used as input to the model. (*b*) Electron temperature profiles and (*c*) the corresponding SXR brightness profiles at times t_1 and t_2, indicated with vertical dotted lines on the figures in the right column. Time evolution of (*d*) χ_e, (*e*) T_e and (*f*) SXR brightness at the radial positions r_1 and r_2, indicated with vertical dotted lines on the figures in the left column.

we show the central χ_e as a function of time. The step-like time variation is evident: in this example χ_e suddenly increases from an initial value of $10\,m^2\,s^{-1}$ up to a final value of $100\,m^2\,s^{-1}$, which will turn out to be in the typical range of values for the perturbed χ_e during MST transient transport events. This sudden perturbation causes the whole electron temperature profile to relax to a new equilibrium, with transient propagation of electron heat from the core towards the edge. This is clear from figure 5(*b*), which shows two T_e profiles at different times: t_1 just before the perturbation is turned on and t_2 during heat propagation. These times are marked by vertical lines on the figures in the right column. After the χ_e perturbation is applied, the electron temperature decreases in the core, while a transient increase is observed in the edge region. An inversion radius at $r_{inv} \simeq 0.33$ m is clearly present, which is larger than that observed in the experimental SXR profiles, $r_{inv} \simeq 0.27$ m. These features are also evident when plotting the electron temperature at different radii as a function of time (see figure 5(*e*)). As expected, T_e pulses are observed at radial positions greater than the inversion radius, r_{inv}. The T_e waveforms reported in figure 5(*e*) correspond to the radial positions r_1 and r_2, marked with vertical lines on the figures in the left column.

To model the SXR measurements we have computed the SXR brightness profiles predicted by the numerical model. In these MST plasmas the SXR emissivity has the following measured dependences: $E_{SXR}(r,t) \propto A(r) n_e^2(r,t) T_e^{\alpha}(r,t)$, with $\alpha \approx 3$. The functions $n_e(r,t)$ and $T_e(r,t)$ have been taken as the outputs of the model. $A(r)$, the so called enhancement factor, is a smoothly increasing function of radius and is assumed not to depend on time during the burst. This is an empirical way of accounting for a different impurity content and/or a different ionization equilibrium among the edge and the core plasma. In our case, an enhancement factor profile that varies linearly from $A = 1$ in the core to $A \simeq 3$ at the edge is needed in order to better fit the amplitude of the experimental SXR peaks. Even if the above assumptions are specific to the present model, we recall here that the main results of the model do not sensibly depend on the detailed shape of the enhancement factor profile and on the choice of the α exponent for the electron temperature in the SXR emissivity formula. This will be shown with more detail in the following.

Starting from the model emissivity function, $E_{SXR}(r,t)$, we have computed the SXR brightness, $B_{SXR}(p,t)$, for different impact parameters, p, as a function of time. Results are reported in figures 5(*c*) and (*f*): the SXR brightness profiles have a time and spatial evolution similar to that of the electron temperature. Some important differences are nonetheless present. First of all, the SXR brightness profiles are more peaked in the core than are the electron temperature profiles: this is both an effect of the chord line integration and of the strong dependence of the SXR emissivity on T_e. These two effects also contribute to shifting the inversion radius, r_{inv}, of the SXR brightness profile with respect to that of the temperature profile towards a value $r_{inv} \simeq 0.3$ m, which is closer to that determined experimentally ($r_{inv} \simeq 0.27$ m). Note also that the shapes of the pulses are different for the temperature and the SXR brightness: the SXR brightness pulses always tend to be more temporally localized than the temperature pulses, which is also due to a line integration effect. This also turns out to be more consistent with experimental signals: the half-height duration of an experimental SXR pulse is in fact on average $\Delta t \simeq 0.3$ ms, while for the modelled temperature pulse $\Delta t \simeq 1$ ms and for the modelled SXR pulse $\Delta t \simeq 0.5$ ms. The model reproduces most of the features of transient transport events observed in experiment and can therefore be used to give an estimate of the perturbed heat diffusivity, χ_e, in these plasmas. In fact, χ_e is a critical parameter in determining the t_p versus r_p^2 dependence.

3.4. Time-to-peak plots predicted by the model

In figure 6(*a*) we present the t_p–r_p^2 plots predicted by our model for the electron temperature pulses at different values of the perturbed χ_e: 50, 100, 150 and $200\,m^2\,s^{-1}$. All of the t_p–r_p^2 curves are linear to a good approximation, and, as expected, the slope of the linear fit increases along with the value of the perturbed χ_e. A similar result is also found for the t_p–p^2 relation computed from the model SXR brightness pulses (see figure 6(*b*)), but we find that the slopes of the linear fits are different for the two types of signals. This is a diagnostic effect and is due to the fact that SXR measurements are line integrated. The SXR brightness mixes regions of plasma at different radii and hence at different electron temperature. This can be important near the edge, where the SXR emissivity gradient is large.

The slope, m, of the linear relation $t_p \propto m r_p^2$ (or $t_p \propto m p^2$ for line-integrated measurements) is a function of χ_e. Under

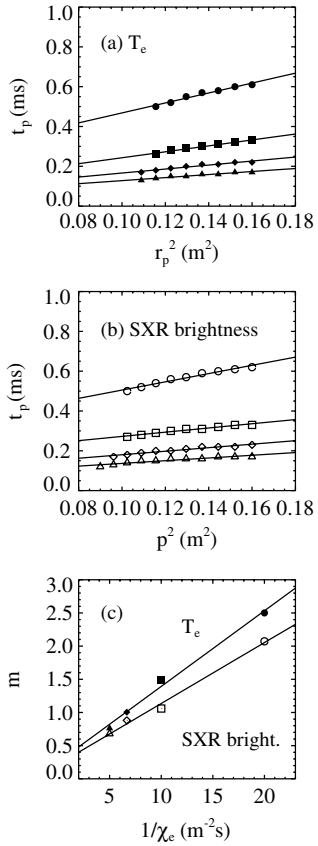

Figure 6. (*a*) t_p–r_p^2 plots for the electron temperature (full symbols) and (*b*) t_p–p^2 plots for the SXR brightness (empty symbols) as predicted by the numerical model for four values of the perturbed χ_e: 50 (circles), 100 (squares), 150 (diamonds), and 200 $m^2\,s^{-1}$ (triangles). (*c*) The constant m defined in equation (3) as computed from linear fits of the above plots versus $1/\chi_e$. The black lines represent linear fits.

our model assumptions, a linear relation holds between the slope, m, and $1/\chi_e$, as shown in figure 6(*c*):

$$t_p \propto m r_p^2 = \frac{C}{\chi_e} r_p^2. \tag{3}$$

The constant C can be computed from a linear fit: for electron temperature pulses we find that $C_{T_e} = 0.11$, while for SXR brightness $C_{SXR} = 0.09$. The value $C_{T_e} = 0.11 \simeq 1/9$ is consistent with that found for the electron temperature in previous analytical and numerical works dedicated to tokamak plasmas [4], thus suggesting that the diffusion process itself could be rather independent of the details of the initial conditions. In contrast, the different value $C_{SXR} = 0.09$ for the SXR brightness can introduce a significant difference when estimating χ_e from experimental data.

3.5. Test of the model sensitivity

Different runs of the above numerical model have been performed using rather different initial conditions, in order to test the sensitivity of the above results on these details. All these runs confirm that the model predictions on the constants C are rather robust and do not depend strongly on the details of the background plasma. We have varied in a wide range the shapes and the absolute values of the electron temperature profile. The shape of the electron temperature profile has been varied from a peaked one, like $T_{e0} = T_0(1 - r^2)^2$, to a flatter one, such as $T_{e0} = T_0(1 - r^6)^6$: the maximum relative variation in the constant C is 8% for electron temperature and 15% for SXR brightness. By varying the value of the central electron temperature, T_0, in the range from 400 to 1000 eV, we have obtained a maximum variation of C of 10% for both electron temperature and SXR brightness. The variation of the exponent α in the SXR emissivity formula in a range from $\alpha \simeq 2$ (which corresponds to Bremsstrahlung emission passing through a 16 μm thick Be filter, which is the filter used for these experiments) to $\alpha \simeq 4$ introduces a variation of the constant C smaller than 2%. A range of α values from 2 to 4 includes all the possible cases for MST. A variation of the enhancement factor profile from a constant one to a linearly increasing one, like that used in the present work, introduces a variation of the constant C smaller than 4%. All these values are smaller than typical experimental errors, as will be shown in the following.

Possible effects on the predictions for the constants C due to the plasma resistivity dependence on electron temperature, and the consequent variation of the ohmic input power across transient transport events, have been investigated assuming a Spitzer dependence of the resistivity, $\eta \propto T_e^{-3/2}$. The transport simulation has been run under two simplifying assumptions: (i) constant applied electric field, i.e. $\boldsymbol{E} = \eta \boldsymbol{j} = \text{const}$, which implies that $\eta j^2 = \eta(\boldsymbol{E}/\eta)^2 \propto T_e^{3/2}$; and (ii) constant current density, i.e. $\boldsymbol{E}/\eta = \boldsymbol{j} = \text{const}$, which implies $\eta j^2 \propto T_e^{-3/2}$. In both cases the constants C have been computed and values very similar to those obtained under the constant ohmic input power assumption have been found, the percentage variation amounting at most to 5%.

4. Estimate of χ_e in perturbed PPCD plasmas

After having tested the robustness of our model, we have used its predictions to estimate a value of the perturbed χ_e for a database of SXR pulses in MST PPCD plasmas with transient transport events. These estimates have been obtained from the Monte Carlo fits of the experimental data introduced above. As explained before, this fit procedure allows one to compute both the slope of the $t_p \propto mp^2$ relation and its standard error. The constant C introduced above can then be directly used to obtain the χ_e values and their standard error. For a database of 18 SXR pulses, we have found χ_e values in a range between 40 and 200 $m^2\,s^{-1}$, with standard errors varying from 15% to 30%. These values are greater than the maximum variation in the constant C predicted by the model.

The estimated χ_e has to be considered as a spatial average of the actual χ_e profile over the radial region spanned by the four edge SXR chords. In figure 7 we show the χ_e radial profiles obtained using the power balance method in standard and PPCD MST discharges at the same value of plasma current $I_p = 400$ kA and electron density $n_e = 1 \times 10^{19}\,m^{-3}$ as the ones included in the present analysis, but without perturbative events (figure adapted from [27]). A green box represents both the distribution of the χ_e values obtained using the perturbative method and the radial region where this estimate extends. The ordinates of the green box are the 25th, 50th and 75th percentiles of the distribution of χ_e, while the two bars are the

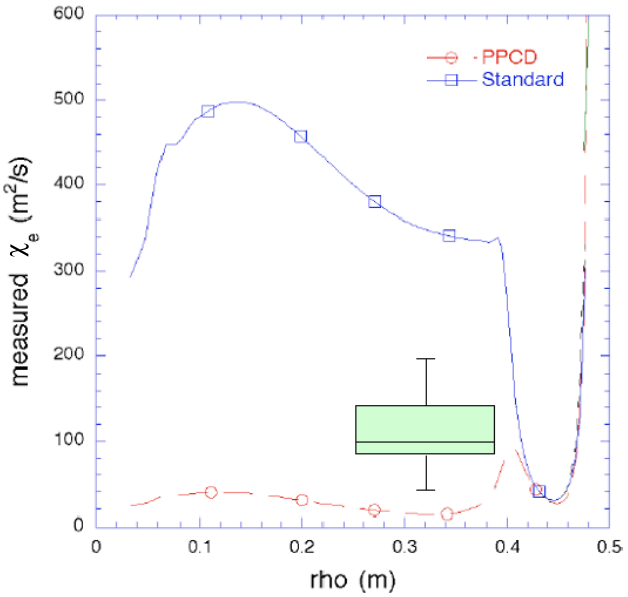

Figure 7. Radial profiles of χ_e computed using the power balance method in 400 kA standard shots (blue line) and in PPCD shots without MHD bursts (red line). Power balance data have been adapted from [27]. The green box represents χ_e values estimated using the perturbative method in similar PPCD shots during MHD bursts. The box ordinates indicate the 25th, 50th and 75th percentiles of the χ_e distribution. The two bars show instead the minimum and maximum χ_e measured values.

minimum and maximum measured χ_e values. The χ_e values obtained using the perturbative method are about ten times larger than those from power balance.

As introduced in section 2, the heat pulses studied here are accompanied by a burst of magnetic fluctuations extending over a broad frequency range. A larger level of magnetic turbulence could thus be responsible for an increased heat conductivity during these events. Nonetheless, as explained in [2, 29], such a difference could also be introduced by non-linear thermal transport models, e.g. by a power dependence of χ_e on T_e, ∇T_e, or the electron heat flux, q_e. Such an effect cannot be ruled out at present due to the absence of a time-resolved diagnostic of the electron temperature profile, but it could be the subject of future work. Nonetheless, it is important to note that during these transient transport events χ_e does not reach values as large as in standard discharges ($\chi_e \simeq 400\,m^2\,s^{-1}$), which is consistent with a less than 30% perturbation of the core electron temperature. Moreover, the timescale of the perturbation is much shorter than the energy confinement time $\tau_E \simeq 10$ ms in PPCD plasmas. As a result, MHD bursts during PPCD experiments do not cause dramatic effects on plasma confinement.

A reasonable agreement has been found between the experimental SXR data and our numerical model. Further improvements in the present model could permit us to reproduce more precisely the experimental SXR signals: (i) the present assumption of a flat χ_e radial profile could be too simple, especially during the bursts, and different shapes could be used; (ii) the time dependence of χ_e could also be modified, for example by introducing a time evolution which fits that of the magnetic mode amplitudes resonant at different radial positions; (iii) a more detailed knowledge of the initial equilibrium profiles could be useful in general in increasing the precision of the model. SXR diagnostic developments are under preparation and could hopefully be available in the future [30].

5. Conclusions

In conclusion, we have studied transient transport phenomena in an RFP using experimental and numerical techniques. A diffusive heat transport model has allowed us to obtain an estimate of the perturbed χ_e during these events, which has been compared with the value measured using the power balance method in an unperturbed situation. Transient transport events in enhanced confinement MST plasmas are correlated with bursts of MHD activity, which extend over a broad range of frequencies and wavenumbers. The discrepancy among the power balance and perturbative estimate could be related to the different level of magnetic fluctuations in the two cases, but an explanation in terms of non-linear thermal transport models cannot be excluded [1, 2, 22]. The estimated χ_e values suggest nonetheless that these perturbed PPCD plasmas are characterized by a reduced level of thermal transport with respect to standard RFP plasmas, thus showing that a reduction of overall thermal transport characterizes also perturbed PPCD plasmas. We have discussed the problem of measuring the perturbed χ_e from line-integrated SXR data in comparison with local electron temperature measurements. We have found that a significant difference can be present between the two estimates, which has been taken into account in the estimation of χ_e.

The present techniques need optimization of both the diagnostic and modelling methods; nevertheless, the results indicate that transient transport experiments are a promising method of studying enhanced confinement RFP regimes. To this purpose, it would be particularly important in future experiments to develop techniques for active induction of small perturbations of electron temperature and/or electron density profiles, like laser blow-off of impurities or injection of small pellets, which have given important results in tokamaks and stellarators experiments. At the same time, comparison of spatially and temporally resolved measurements of SXR emissivity, electron temperature and density profiles could help in further improving the interpretation of these events.

Acknowledgments

We acknowledge the strong, continuous scientific support of the whole MST team and in particular of D. Craig, J.S. Sarff and S.C. Prager, whose contributions were important to the success of this project. We would like to thank J.D. Callen and D.F. Escande for very stimulating discussions. We also thank M.E. Puiatti for her help in reviewing and improving the manuscript and M. Reyfman for technical support with the SXR diagnostics.

References

[1] Lopes Cardozo N.J. 1995 *Plasma Phys. Control. Fusion* **37** 799
[2] Stroth U. 1998 *Plasma Phys. Control. Fusion* **40** 9

[3] Callen J.D. and Jahns G.L. 1977 *Phys. Rev. Lett.* **38** 491
[4] Soler M. and Callen J.D. 1979 *Nucl. Fusion* **19** 703
[5] Fredrickson E.D. *et al* 1986 *Nucl. Fusion* **26** 849
[6] DeBoo J.C. *et al* 1999 *Nucl. Fusion* **39** 1935
[7] Galli P. *et al* 1998 *Nucl. Fusion* **38** 1355
[8] Carolan P.G., Patel A., Sexton M.C. and Walsh M.J. 1990 *Nucl. Fusion* **30** 2616
[9] Callen J.D. and Kissick M.W. 1997 *Plasma Phys. Control. Fusion* **39** B173
[10] van Milligen B.P. *et al* 2002 *Nucl. Fusion* **42** 787
[11] Parail V.V. *et al* 1997 *Nucl. Fusion* **37** 481
[12] Mantica P. *et al* 2002 *Plasma Phys. Control. Fusion* **44** 2185
[13] Dexter R.N. *et al* 1991 *Fusion Technol.* **19** 131
[14] Ortolani S. and Schnack D.D. 1993 *Magnetohydrodynamics of Plasma Relaxation* (Singapore: World Scientific)
[15] Xiao C. *et al* 2003 *Rev. Sci. Instrum.* **74** 2157
[16] Wurden G. 1984 *Phys. Fluids* **27** 551
[17] Watt R.G. and Little E.M. 1984 *Phys. Fluids* **27** 784
[18] Sarff J.S., Lanier N.E., Prager S.C. and Stoneking M.R. 1997 *Phys. Rev. Lett.* **78** 62
[19] Chapman B.E. *et al* 2001 *Phys. Rev. Lett.* **87** 205001
[20] Franz P. *et al* 2003 *Rev. Sci. Instrum.* **74** 2152
[21] Biewer T.M. *et al* 2003 *Phys. Rev. Lett.* **91** 045004
[22] Sarff J.S. *et al* 2003 *Nucl. Fusion* **43** 1684
[23] O'Connell R. *et al* 2003 *Phys. Rev. Lett.* **91** 045002
[24] Franz P. *et al* 2004 *Phys. Rev. Lett.* **92** 125001
[25] Den Hartog D.J. *et al* 1999 *Phys. Plasmas* **6** 1813
[26] Schiesser W.E. 1991 *The Numerical Method of Lines: Integration of Partial Differential Equations* (San Diego: Academic)
[27] Biewer T.M. 2002 Electron thermal transport in the Madison Symmetric Torus *PhD Thesis* University of Wisconsin–Madison
[28] Martin P., Murari A. and Marrelli L. 1996 *Plasma Phys. Control. Fusion* **38** 1023
[29] Stroth U. *et al* 1996 *Plasma Phys. Control. Fusion* **38** 611
[30] Franz P. *et al* 2004 *Rev. Sci. Instrum.* **75** 4013